BBA - General Subjects 1863 (2019) 342–350

Contents lists available at ScienceDirect

BBA - General Subjects

journal homepage: www.elsevier.com/locate/bbagen

Interaction of the anticancer p28 peptide with p53-DBD as studied by fluorescence, FRET, docking and MD simulations

Anna Rita Bizzarri, Ilaria Moscetti, Salvatore Cannistraro*

Biophysics and Nanoscience Centre, DEB, Università della Tuscia, Viterbo, Italy

ARTICLE INFO

Keywords:
p53
Anticancer peptides
Fluorescence
FRET
Computational docking

ABSTRACT

Background: The p28 peptide, derived from the blue copper protein Azurin, exerts an anticancer action due to interaction with the tumor suppressor p53, likely interfering with its down-regulators. Knowledge of both the kinetics and topological details of the interaction, could greatly help to understand the peptide anticancer mechanism.

Methods: Fluorescence and Förster resonance energy transfer (FRET) were used to determine both the binding affinity and the distance between the lone tryptophan (FRET donor) of DNA Binding Domain (DBD) of p53 and the Iaedens dye (FRET acceptor) bound to the p28 peptide. Docking, Molecular Dynamic simulations and free energy binding calculations were used to single out the best complex model, compatible with the distance measured by FRET.

Results: Tryptophan fluorescence quenching provided a $10^5\,M^{-1}$ binding affinity for the complex. Both FRET donor fluorescence quenching and acceptor enhancement are consistent with a donor-acceptor distance of about 2.6 nm. Docking and molecular dynamics simulations allowed us to select the best complex, enlightening the contact regions between p28 and DBD.

Conclusions: p28 binds to DBD partially engaging the L1 loop, at the same region of the p53 down-regulator COP1, leaving however the DNA binding site available for functional interactions.

General significance: Elucidation of the DBD-p28 complex gets insights into the functional role of p28 in regulating the p53 anticancer activity, also offering new perspectives to design new drugs able to protect the p53 anticancer function.

1. Introduction

The transcription factor p53 is at the center of a complex cellular network and plays a well-known tumor suppressor activity [1]. In healthy cells, levels of p53 are kept low by a tight regulation of a series of ubiquitin E3 ligases (mainly HDM2 (human double minute 2) [2] and COP1 (constitutively photomorphogenic 1) [3] that bind p53, promoting its proteasomal degradation [4]. In response to stress signals, post-translational stabilization of p53 leads to an increase of its intracellular levels, resulting in the activation of gene transcription for DNA repair, cell cycle arrest and apoptosis [5]. Since the p53 onco-suppressive function is inactivated in many human cancers, mainly by mutations or by dysregulation of the ubiquitin-proteasome pathway, large efforts are currently devoted to identify, design and potentiate molecules able to stabilize or to restore the anticancer activity of p53 [6–8]. Among other molecules, the cupredoxin Azurin, from *Pseudomonas Aeruginosa* bacterium, has been found to preferentially enter cancer cells and to form a specific and stable complex with p53, with a concomitant increase of its tumor suppressor activity [9–13]. Interestingly, the peptide, called p28, formed by the α-helix fragment (50 to 77 AA) of Azurin is an extremely promising molecule inheriting the overall tumoricidal activity of Azurin, but with less side effects [14]. Indeed, p28, which is characterized by an efficient cellular penetration ability, can bind p53 leading to an enhancement of its intracellular levels [13]. The interaction between p28 and full-length p53 or its isolated domains (DNA-binding domain (DBD) and the N-terminal domain (NTD)), has been established by different approaches [15–17]. In particular, Atomic Force Spectroscopy (AFS) has allowed to determine the unbinding force and the dissociation rate constant between p28 and DBD or NTD, at single molecule level [15]. Furthermore, the kinetics of the DBD-p28 complex formation has been characterized in bulk by Surface Plasmon Resonance (SPR) [18]. However, a detailed information about the topography and the contact regions of the DBD-p28 complex, is still missing. Indeed, such a knowledge could be of utmost importance to

* Corresponding author.
E-mail address: cannistr@unitus.it (S. Cannistraro).

https://doi.org/10.1016/j.bbagen.2018.11.003
Received 19 July 2018; Received in revised form 7 November 2018; Accepted 7 November 2018
Available online 10 November 2018

better understand the mechanisms regulating the anticancer action of p28, also in connection with the down-regulation pathway of p53 as well as its interference with the DNA binding capability for gene regulation. Additionally, insights could be also gained to refine the p28 molecule in order to potentiate its anticancer capabilities, and in the perspective of designing new drugs targeting the p53 pathway. With such an aim, we have investigated the interaction between the p28 peptide and the DBD region of p53, by applying fluorescence and Förster resonance energy transfer (FRET) techniques combined with computational docking and molecular dynamics (MD) simulations. By titration fluorescence experiments, we have assessed the formation of a stable complex between DBD, containing a single tryptophan (Trp146), and p28 by also determining the binding affinity. FRET experiments, carried out using DBD, whose loneTrp146 constitutes the fluorescent donor, and a p28 peptide labelled with a suitable dye acting as acceptor, have allowed to estimate the distance between the donor and the acceptor. Models for the DBD-p28 complexes, extracted by computational docking, have been refined by Molecular Dynamics (MD) simulations, binding free energy calculations, and then validated by the measured FRET distance. The best models found for the DBD-p28 complex have revealed that the p28 peptide engages a region close to the L1 loop of DBD, which is the same binding region of the p53 down-regulator COP1, and leaves the DNA binding domain available for interaction. These results are briefly discussed in connection with the functional role of p28 in regulating the p53 anticancer activity, and in the perspective of helping design of new drugs with enhanced p53 anticancer function.

2. Methods

2.1. Materials

Recombinant human p53 DNA binding domain (DBD) residues 94–300 (23.4 kDa) was purchased from GenScript (Piscataway, NJ, USA) by using the BacPower™ Guaranteed Bacterial Protein Expression Service. The identity and purity of DBD were verified by SDS-PAGE analysis (> 90% purity) and by Mass Spectrometry (MS) (73% coverage) by the manufacturer. and by Mass Spectrometry (MS) (73% coverage). The p28 peptide (LSTAADMQGVVTDGMASGLDKDYLKPDD, 2914 Da), with the addition of a cysteine residue at the N-terminal (hereafter p28), was synthesised and verified by MS and HPLC (93% purity) by GenScript (Piscataway, NJ, USA).

1.5-Iaedans (5-({2-[(iodoacetyl)amino] ethyl}amino) naphthalene-1-sulfonic acid, IAD) was purchased from Molecular Probes (ThermoFisher Scientific, Waltham, Massachusetts, USA). Phosphate Buffered Saline (PBS), 50 mM at pH 7.4, hereafter PBS buffer, was prepared by using reagents from Sigma Aldrich (Saint Louis, Missouri, US).

2.2. Preparation of p28IAD

The labelling of p28 was performed by covalent coupling the IAD dye at the p28 N-terminal cysteine by using the procedure described in ref. [19]. Briefly, 100 μM of p28 in buffer (PBS 50 mM pH 7.4) were incubated with twenty fold molar excess of IAD overnight at 4 °C. Extensive dialysis against PBS buffer for 36–48 h by means of Slide-A-Lyzer™ G2 Dialysis Cassettes (ThermoScientific) with a cutoff of 2000 kDa and 4 to 6 buffer changes were performed to remove excess of IAD. Dialysis was stopped when the IAD fluorescence emission at 439 nm of washing buffer excited at 337 nm was no longer detected. The p28 concentration after dialysis was determined from the fluorescence emission at 308 nm of the p28IAD sample, excited at 280 nm, by using the calibration curve obtained for p28 in the 5–45 μM concentration range. Additionally, the amount of the labelled p28IAD sample after dialysis was determined by the absorption at 337 nm, using a molar extinction coefficient of 5700 $mM^{-1} cm^{-1}$ [20]. Typically, the labelling stoichiometry, f_a, defined as the moles of dye per mole of molecule, was about 0.5.

2.3. Spectroscopic measurements and data analysis

Absorbance spectra were recorded at room temperature by a double beam Jasco V-550 UV/visible spectrophotometer by using 1 cm path length cuvettes and 1 nm bandwidth in the spectral region 220–750 nm, using PBS buffer as reference. Steady-state fluorescence measurements were performed with a FluoroMax®-4 Spectrofluorometer (Horiba Scientific, JobinYvon, France). Samples were excited at 295 nm and fluorescence emission was collected from 305 to 580 nm by using 1 nm increments and integration time of 0.50 s. A 2 nm bandpass was used in both excitation and emission paths. Spectra were acquired in the signal to reference (S/R) mode to take into account for random lamp intensity fluctuations. Moreover, emission spectra were corrected for Raman contribution from the buffer. For each fluorescence experiment, ten measurements were performed on independently prepared samples by determining the average and the corresponding standard deviation. Lifetime measurements were performed at room temperature with the time-correlated single photon counting method using FluoroMax®-4 Spectrofluorometer (Horiba Scientific, Jobin Yvon, France), operating at a repetition rate of 1 MHz and running in reverse mode. The apparatus was equipped with a pulsed nanosecond LED excitation head at 295 nm (Horiba Scientific, Jobin Yvon, France) having a temporal width lower than 1 ns and a bandwidth of 4 nm. Detection was at 345 nm and the fluorescence lifetime data were acquired until the peak signal reached 10,000 counts. Time-resolved fluorescence decays were analysed making use of the impulse response function (DAS6 software, Horiba Scientific, Jobin Yvo, France). The function describing the fluorescence decay was assumed to be a sum of exponential components and data were analysed by employing a non-linear least square analysis including deconvolution of the prompt. The goodness of the fit was evaluated in term of both χ^2 value and weighted residuals.

2.4. Structure of DBD

The structure of DBD (see Fig. 1A) was derived from the chain B from the protein data bank (PDB) entry 1 TUP, in complex with a consensus DNA [21]. DBD is characterized by a β-sandwich structure formed by two antiparallel β-sheets made up of four and five strands, respectively. The β-sandwich acts as a scaffold for the L2 and L3 loops, and for a loop-sheet–helix motif (L1 − H2). L2 and L3 are connected by a zinc ion, which is coordinated by the side-chains of the residues

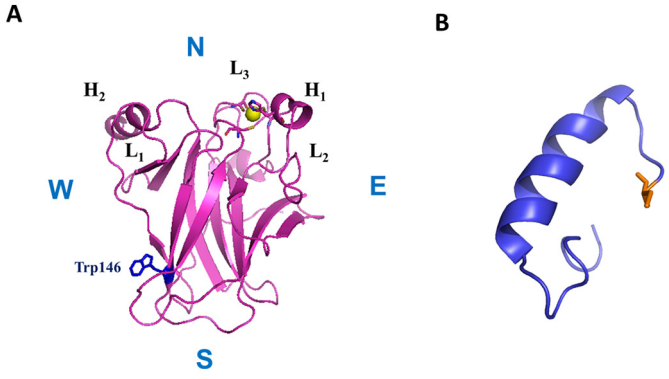

Fig. 1. A) Three-dimensional structure of DBD (chain B of 1TUP pdb entry). The zinc ion is represented as a yellow sphere and its coordinated residues are marked as sticks. The Trp146 residue is marked as blue sticks. The regions around the DBD molecule are labelled as follows: northern (N), southern (S), western (W) and eastern (E). B) Structure of the p28 peptide as derived from the α-helix of Azurin (chain B of 4AZU pdb entry), with the addition of a cysteine residue at the N-terminal, marked as sticks in orange.

Cys176, His179, Cys238, and Cys242, forming a zinc-finger motif [22]. The functional binding to the DNA of DBD occurs within L1 and L3 loops in a region, conventionally chosen to be the northern part (N) of the molecule; the other part of the molecules being also marked in Fig. 1A (for a more extended description see ref. [23]).

2.5. Modelling of p28

The p28 peptide is derived from the 50–77 AA of the chain B Azurin structure, PDB entry 4AZU [24], including the α–helix region (54 to 67AA) and a small part of a β–sheet (68-77AA). A Cys residue, suitable to bind a label was added to its N-terminal by using the SPDBV 4.10 software [25]; the resulting peptide (called analogously p28) being shown in Fig. 1B. By taking into consideration that Circular Dicroism (CD) and Raman spectroscopy showed that p28 is characterized, in water, by random coils [26], the p28 Azurin-derived structure, was relaxed by a 5 ns long MD run at 330 K in water, followed by a 50 ns long run at 300 K. The peptide rapidly unfolded by assuming slightly different random coil conformations, with occasional formation of short β-sheet portions. Such a structural heterogeneity of p28 finds a correspondence with experimental Raman data [27]. Snapshots of p28, extracted from the last 5 ns of the 50 ns run at steps of 0.1 ns, were analysed and grouped according to their secondary structure; the models with the highest occurrence, labelled as p28_M1, p28_M2, …p28_M10, having been shown in Fig. 2.

2.6. Docking procedures

The structure of the DBD-p28 complex was modelled by a docking procedure starting from the DBD structure and the p28_M1 - M10 models, by applying *Z*-Dock 3.0 [28], which is a rigid-body docking algorithm which uses Fast Fourier Transform for a six-dimensional search in the translational and rotational space between the two biomolecules. For each of the ten different p28 models (p28_M1-M10), ten best models for the DBD-p28 complex were generated and analysed.

2.7. Molecular dynamics simulation procedures

MD simulations of p28, DBD and the DBD-p28 complexes in water were carried out by the GROMACS 5.1.2 package [29,30], including GROMOS96 43a1 Force Field for the protein [31], and the SPC/E for water [32]. Each molecular system was centered in a box with dimensions: $6.5 \times 6.5 \times 6.5\,nm^3$ for p28; $8.0 \times 7.5 \times 7.5\,nm^3$for DBD; and $10.0 \times 10.0 \times 10.0\,nm^3$ the DBD-p28 complex. Each box was filled with water molecules, by assuring a minimum hydration level of 9 g water/g protein. The residues were assumed to be in the ionization states expected at pH 7 by taking into consideration their standard pKa values. The systems were kept electrically neutral by eventually adding Cl- or Na + ions. In all the simulations, the cutoff radius of both electrostatic and van der Waals interactions were set at 0.9 nm and the neighbour list was updated every 10 steps. The Particle Mesh Ewald (PME) method [33,34] was used to calculate the electrostatic interactions with a lattice constant of 0.12 nm and using fourth order cubic spline interpolation. H bonds were constrained with the LINCS algorithm [35]. Periodic Boundary Conditions in the NPT ensemble with $T = 300$ K and $p = 1$ bar, with a time step of 1 fs were used. The Nosé-Hoover thermostat was used to control the system temperature, with a coupling time constant $\tau_T = 0.1$ ps [36], while constant pressure was imposed according to Parrinello-Rahman extended-ensemble [37], with a time constant $\tau_P = 2.0$ ps. After energy minimization, each system was heated from 50 K to 300 K with two intermediate steps at 150 K and 250 K. The trajectories were analysed by the GROMACS package tools [30]. All the protein structure figures of were created by Pymol [25] and VMD [38]. Analysis of both the secondary structure and Surface Accessible Surface (SAS) of the molecules was carried out by DSSP [39].

2.8. Calculation of the binding free energy

The binding free energy of the DBD-p28 complex was evaluated by the Molecular Mechanics Poisson-Boltzmann Surface Area (MM-PBSA) method, following the procedures reported in refs [40–42].. Briefly, the binding free energy, ΔG_B, between a ligand and receptor forming a complex, was estimated from: $\Delta G_B = G_{complex} - G_{receptor} - G_{ligand}$, where each free energy term, G, can be calculated as:

$$G = E_{MM} - TS_{MM} + G_{solv} \quad (1)$$

where E_{MM} is the internal energy, TS_{MM} is the entropic term and the G_{solv} the solvation contribution. The E_{MM} energy can be described as $E_{MM} = E_{elec} + E_{VdW}$, where the two terms represent the protein-protein electrostatic and Van der Waals interaction energies, respectively. The entropic contribution was evaluated, for the different docking models, by the quasi-harmonic approach reported in refs. [43, 44]. The solvation term G_{solv} can be further decomposed into electrostatic ($G_{polar,solv}$) and non-polar ($G_{non\ polar,solv}$) parts [45]. The former was obtained by numerically solving the Poisson–Boltzmann equation with the Adaptive Poisson–Boltzmann Solver (APBS) software [46]. The grid-spacing was set to 0.25 Å. The GROMOS96 43a1 force field parameter set was used for atomic charges and radii; a probe radius of 1.4 Å was used to define the dielectric boundary. The interior dielectric constant for the complexes was 4 and the water dielectric constant was set to 80 [47]. The non-polar contribution to G_{solv} was assumed to be proportional to the SAS: $G_{non\ polar,solv} = \gamma\ SAS + \beta$, with $\gamma = 2.2\,kJ\,mol^{-1}\,nm^{-2}$ and $\beta = 3.84\,kJ\,mol^{-1}$ [48]. For each complex, the free energy was

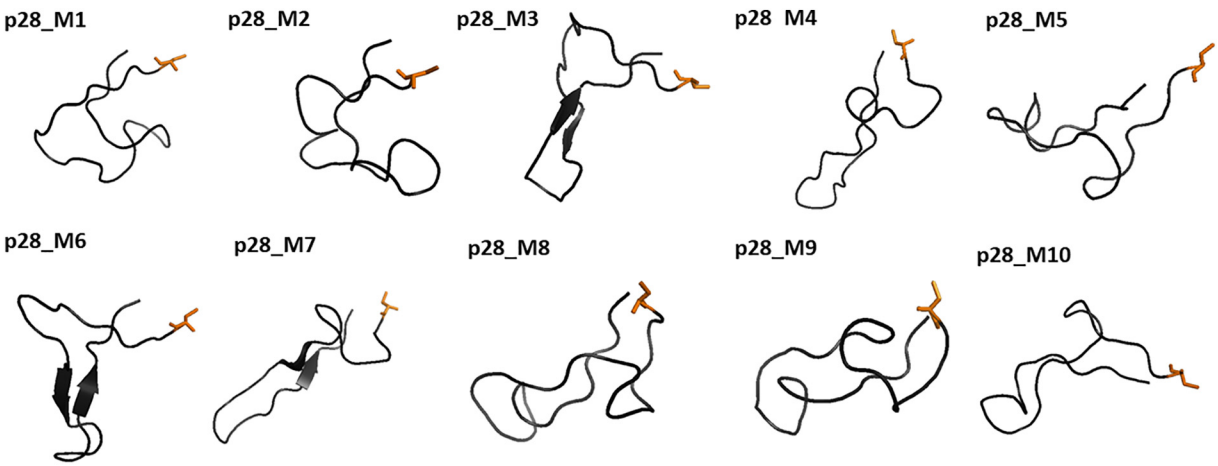

Fig. 2. Ten models for the p28 peptide; Cys1, at N-terminal, being marked as sticks in orange.

evaluated by averaging over 100 snapshots, recorded every 0.1 ns from the last 1 ns of the MD simulation runs.

2.9. Structural cluster analysis

A cluster analysis of MD trajectories were performed by the method described in ref. [49] and implemented in GROMACS (tool Cluster) [29]. Such a method allows one to group similar molecular structures from the simulated trajectories by using a RMSD cutoff value; with the representative structure in the cluster being defined as that one with the lowest average RMSD within the other structures belonging to the same cluster. Clustering was performed by an all atoms RMSD cutoff by using values ranging from 0.10–0.15 nm with a step of 0.01 nm. By passing from 0.10 nm to higher cutoff values, the number of clusters collapses, and a few structures describe the trajectories. Therefore, for a more detailed cluster analysis, a RMSD cutoff of 0.10 nm was used.

3. Results and discussion

3.1. Fluorescence quenching and FRET experiments

Fig. 3 shows the emission spectrum of DBD in solution (black line), obtained by excitation at 295 nm, at which its single tryptophan residue (Trp146) still absorbs, while the Tyr and Phe residues are not substantially excited. The spectrum is peaked at about 345 nm (see the arrow), indicating that Trp146 is almost fully exposed to the solvent in agreement with its rather high solvent accessibility surface; a SAS of about 80 $Å^2$ having been measured for Trp146 in the DBD X-ray structure.

The fluorescence emission of DBD, at increasing concentrations of p28 (coloured lines in Fig. 3), is progressively reduced, with no significant wavelength shift of the peak; with this indicating that the solvent exposition of Trp146 to the solvent is not affected by p28.

Fig. 4 shows the F_0/F ratio (black squares), as a function of the p28 concentration, where F_0 and F are the fluorescence emission intensity at 345 nm of DBD in the absence and in the presence of p28, respectively. The plot exhibits a linear trend which can be generally described by the well-known Stern–Volmer equation [50]:

$$\frac{F_0}{F} = 1 + k_q\tau_q[Q] = 1 + K_{SV}[Q] \quad (2)$$

where k_q is the bimolecular quenching constant (or quenching rate constant), K_{SV} is the Stern-Volmer quenching constant, [Q] is

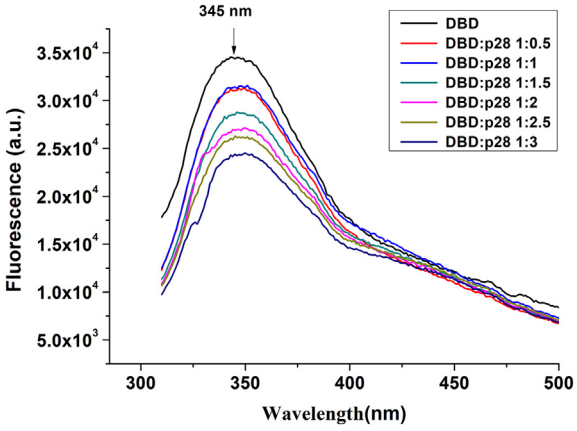

Fig. 3. Fluorescence emission spectra of DBD, at 1 μM, in PBS buffer at pH = 7.4, alone (black line) and in presence of progressively higher concentrations of p28 (coloured lines); the corresponding DBD:p28 ratio having been reported in the inset. The peak of the DBD spectrum, at about 345 nm, is marked by an arrow. All the spectra were obtained by an excitation at 295 nm and corrected for the Raman scattering of the buffer.

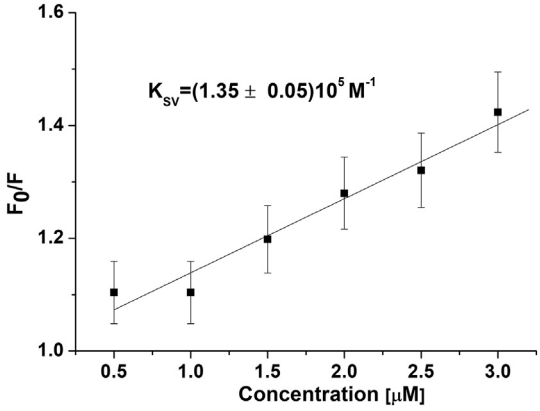

Fig. 4. Stern–Volmer plot of the fluorescence quenching of DBD (fluorophore) as a function of p28 (quencher) concentration (black squares). Continuous black line is the linear fit by Eq. (2); the Stern-Volmer constant, extracted from the fit, being reported.

concentration of the quencher (the p28 peptide in our case) and τ_q is the average lifetime of the fluorophore (DBD Trp146) in the absence of quencher.

From the slope of the linear fit by Eq. (2) (black line in Fig. 4), we have determined a K_{SV} of $(1.35 \pm 0.05)\cdot10^5\,M^{-1}$ and a bimolecular quenching constant $k_q = K_{SV}/\tau_q$ of about $3.3\cdot10^{13}\,M^{-1}\,s^{-1}$, by assuming $\tau_q \sim 10^{-9}$ s [50]. Since the k_q value is much higher than the limiting diffusion constant, ($K_{diff} \sim 1\cdot10^{10}\,M^{-1}\,s^{-1}$ [50]), we could reasonably infer the occurrence of static quenching. In this connection, we have determined the lifetime of the fluorophore (DBD Trp146) in the absence and in the presence of the quencher. We found that the lifetime of DBD in solution is (3.19 ± 0.01) ns which is almost identical to that measured for DBD + p28 solution (at 1:1 ratio the lifetime is 3.17 ± 0.01 ns). Such a result provides an additional evidence to the occurrence of a static quenching mechanism [44].

Therefore, addition of p28 to the DBD solution gives rise to the formation of a stable complex between DBD and p28 with an association constant, K_A, which corresponds to the Stern-Volmer quenching constant K_{SV}. The value measured for K_A is $(1.35 \pm 0.05)\cdot10^5\,M^{-1}$, corresponding to a dissociation constant, $K_D \sim 7.4\cdot10^{-6}$ M. This result is slightly lower than that obtained by the nanotechnological technique, Atomic Force Spectroscopy (AFS), operating at single molecule level, and somewhat lower than that found and by Surface Plasmon Resonance (SPR) in bulk [15,17]. The discrepancy can be ascribed to the different experimental conditions. Indeed, in fluorescence experiments, the molecules are free in solution, while in SPR or AFS experiments, one or both the molecules are stably anchored to a surface and this could result into different binding properties [51]. Since the fluorescence quenching of DBD Trp146, by addition of p28, is not associated to any wavelength shift of fluorescence peak at 345 nm, it could be hypothesized that binding of p28 may induce an allosteric effect, likely via a DBD conformational change, on the Trp fluorescence.

To obtain additional information on the structure of the DBD-p28 complex, we have applied the FRET technique which allows to estimate the distance between a donor (D) and an acceptor (A) from the D-A energy transfer efficiency (E_{FRET}) [50]. In our system, DBD Trp146 is the donor, while IAD bound to p28 peptide is the acceptor. These constitute an appropriate D-A couple for a FRET experiment, because of the high overlapping between the emission spectrum of DBD, excited at 295 nm, as due to Trp146, and the absorption spectrum of IAD [52]. Accordingly, the D-A distance, R, is related to E_{FRET} through the expression [50]:

$$E_{FRET} = \frac{R_0^6}{R_0^6 + R^6} \quad (3)$$

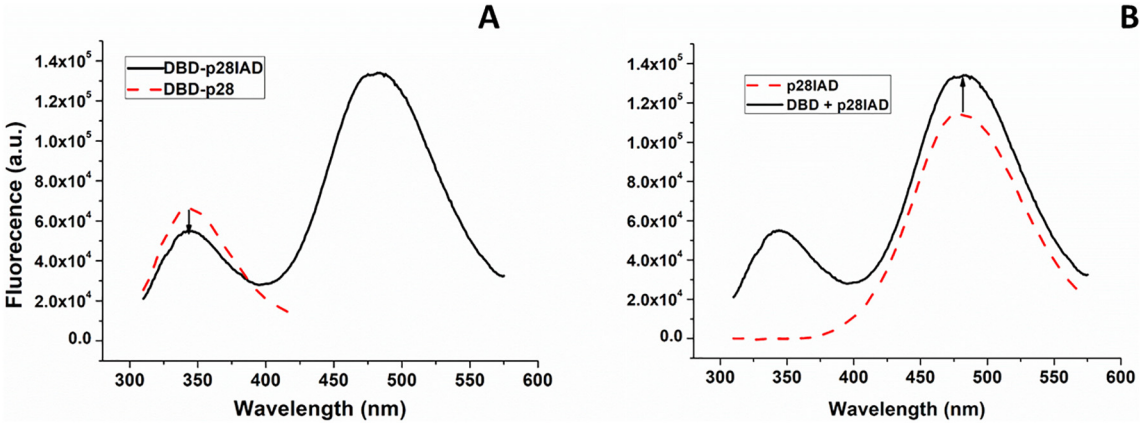

Fig. 5. A) Representative fluorescence emission spectra of DBD + p28 (solid line) and of DBD + p28IAD (dashed red line); both the spectra having been obtained at a concentration of 1 μM with a 1:1 M ratio between DBD and p28 or p28IAD. B) Representative fluorescence emission spectra of p28IAD (dashed red line) at a concentration of 1 μM and of DBD + p28IAD, (solid line) obtained at a concentration of 1 μM and with a 1:1 M ratio between DBD and p28IAD. All the spectra were excited at 295 nm and corrected for the Raman scattering of the buffer.

where the Förster radius, R_0, for this D-A couple is 2.2 nm [53].

To evaluate E_{FRET} in the DBD-p28 system, we have followed two methods based on: i) the fluorescence quenching of D in the presence of A; and ii) the enhancement of the fluorescence emission of A upon exciting D. Fig. 5A shows representative fluorescence emission spectra of DBD-p28 (dashed line), and of DBD-p28IAD (continuous line), excited at 295 nm, at 1:1 molecular ratio in both cases. As previously shown (see Fig. 4), the fluorescence emission spectrum of DBD-p28, peaking at 345 nm, arises only from the excitation of DBD Trp146. On the other hand, the emission spectrum of DBD-p28IAD displays another band, centred at about 480 nm, which results from the direct excitation of IAD, at 295 nm. Notably, in the latter case, the peak at 345 nm is quenched with respect to that of DBD-p28; with this being indicative of an energy transfer from D to A, and of label effects. The corresponding E_{FRET} value can be determined from [50]:

$$E_{FRET} = 1 - \frac{F_{DA}}{F_D f_a} \tag{4}$$

where F_D and F_{DA} are the fluorescence emission intensities, at 345 nm, of DBD-p28 and of DBD-p28IAD, respectively; while f_a is the labelling stoichiometry of p28IAD, estimated to be 0.5 in our samples (see Materials and Methods). Upon measuring F_D and F_{DA}, and combining Eqs.3 and 4, the R parameter, providing the D-A distance, can be determined. From measurements conducted on ten independently prepared samples, a R value of (2.55 ± 0.05) nm has been obtained (see also Table 1).

Fig. 5B shows representative fluorescence emission spectra of DBD-p28IAD (dashed line), and of p28IAD (continuous line), obtained upon excitation at 295 nm. Notably, the fluorescence emission intensity, at 480 nm, due to the IAD bound to p28, is enhanced in the presence of DBD. By taking into account the absorption of IAD alone, E_{FRET} can be evaluated from the following expression [50,52]:

$$E_{FRET} = \left(\frac{F_{AD}}{F_A} - 1\right)\left(\frac{\varepsilon_A}{\varepsilon_D}\right) \tag{5}$$

where F_A and F_{AD} are the fluorescence emission intensities of p28IAD and of DBD-p28IAD, respectively, while are $\varepsilon_A = 3800\ M^{-1}\ cm^{-1}$ and $\varepsilon_D = 1500\ M^{-1}\ cm^{-1}$ are the molar extinction coefficients of A and D, respectively, at the wavelength of 295 nm [19,50,54].

Upon measuring F_A and F_{AD}, Eqs.3 and 5 provide R and then the D-A distance. From measurements of ten independently prepared samples, a value R of (2.55 ± 0.08) nm (see also Table 1) has been obtained. This value is practically the same as that obtained by the fluorescence quenching approach. Fig. 6 shows a circle of radius R centred at the lateral chain of DBD Trp146. According to the FRET results, the IAD acceptor bound to the Sulphur atom of p28 should be located on the portion of circle external to the protein.

Table 1
Average and standard deviations of E_{FRET} and of the distance between the donor (Trp146) and acceptor (p28IAD) (named DA_distance) in the DBD-p28 complex, as obtained from measurements of ten independent samples, by two different FRET methods.

FRET method	E_{FRET}	DA_distance (nm)
D-quenching	0.28 ± 0.03	2.55 ± 0.05
A-enhancement	0.29 ± 0.03	2.55 ± 0.08

3.2. Modelling the DBD-p28 complex

To model the structure of the DBD-p28 complex, we have applied a combined computational approach, based first on a docking study between DBD and p28, followed by a refinement of the complex geometry by both MD simulations and binding free energy calculations. The obtained best models have been then validated by comparing their D-A distance with the experimentally determined value of R. In more detail, the p28_M1-p28_M10 models (see Material and Methods Section and Fig. 2) have been submitted to a rigid docking procedure based on the X-ray structure of DBD (see Fig. 1A). For each p28 model, the first ten ranked complexes have been extracted, obtaining thus a total of a hundred DBD-p28 models. A superposition of all the ten docking models between DBD and the p28_M1 structure is shown in Fig. 7A; while the highest ranked docking models between DBD and ten

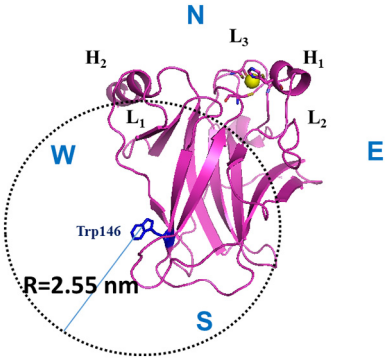

Fig. 6. Schematic representation of the region (dashed line), obtained from the circle centred on the lateral chain of Trp146 of DBD, (donor), with a radius of 2.55 nm, at which the sulphur atom of p28-Cys, binding the dye (acceptor) could be found, according with FRET data.

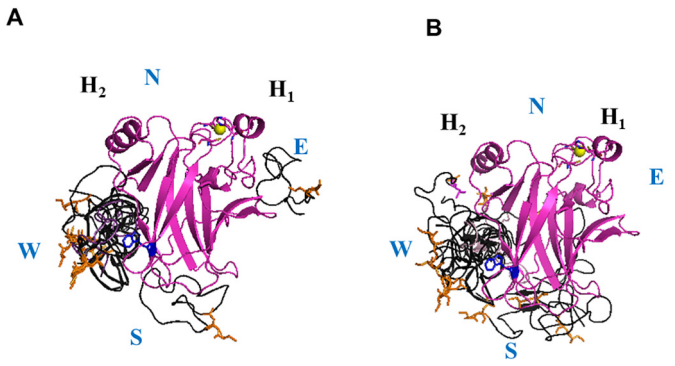

Fig. 7. A) Superposition of the ten models for the DBD-p28 complex obtained by a docking procedure between DBD and the p28_M1 model. B) Superposition of first ranked models for the DBD-p28 complex obtained by the docking between DBD and ten different p28 models (p28_M1-p28_M10). DBD is in magenta while p28 is in black with its Cys1 marked in orange.

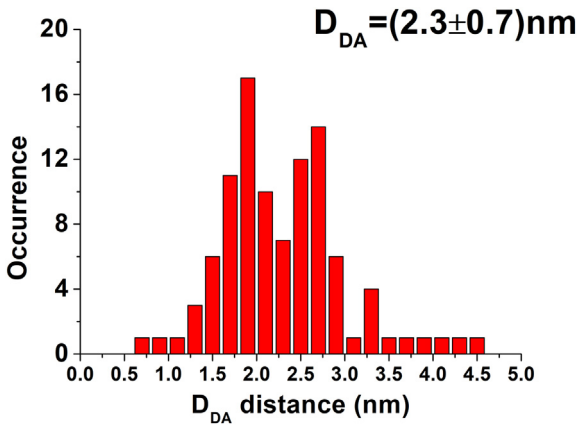

Fig. 8. Histogram of the D_{DA} distance, as extracted from the 100 different docking models for the DBD-p28 complex; the average and the corresponding standard deviation being reported.

different p28 structures (p28_M1-p28_M10) are shown in Fig. 7B. We note in both figures that the p28 peptide most frequently clusters around the western part of DBD (labelled as W region). Collectively, we found that within 86 over 100 docking models, p28 binds at the W region of DBD, while, in 11 complexes, it binds at the S region of DBD.

For each complex, we have measured the distance, labelled by D_{DA}, between the Sulphur of the peptide Cys1, to which the IAD label is bound, and the center of the aromatic rings of the lateral chain of Trp146 belonging to DBD. The histogram of the D_{DA} distances, shown in

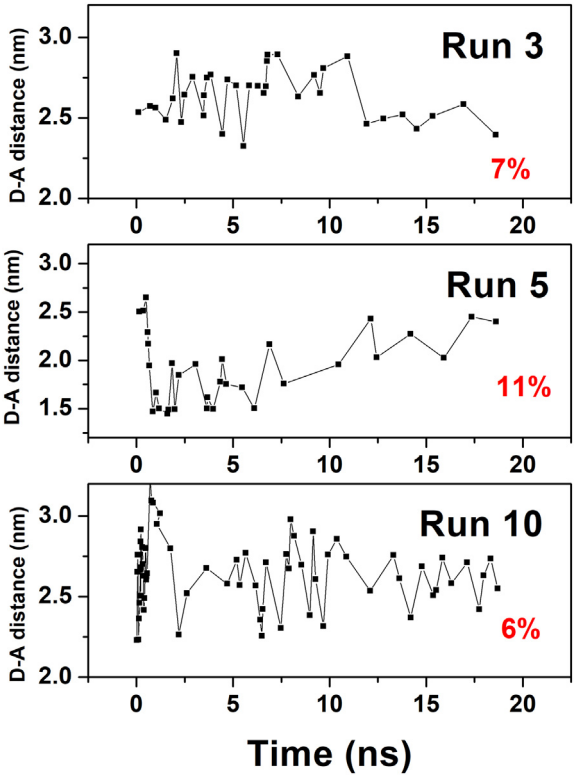

Fig. 10. Temporal evolution of the D_{DA} distance for the structures determined by a clustering analysis with an all atom RMSD cutoff of 0.10 nm, for three runs. The percentage of the structures belonging to the last cluster over the total structures, is reported.

Fig. 8, is characterized by a wide distribution, with values ranging from 0.7 nm to 4.4 nm, with an average value of 2.3 nm and a standard deviation of 0.7 nm. Among all the modelled complexes, only five are characterized by a D_{DA} distance comprised between 2.5 and 2.6 nm, and then reasonably consistent with the R value measured by FRET experiments. To take into account possible structural relaxation, we have submitted the complexes whose D_{DA} distance was comprised in the 2.3–2.7 nm range, to a 20 ns long MD simulations; 16 complexes, labelled as Model_1-Model_16 having been found in such range, which has been chosen as slightly wider than that obtained by FRET.

At the end of the run, we found that Models 3, 5 and 10 are characterized by D_{DA} values within the 2.5–2.6 nm range, and then in a full agreement with the D-A distance value measured by FRET. A graphical representation of these three complexes, together with their corresponding D_{DA} value, is shown in Fig. 9. After the MD run, the D_{DA}

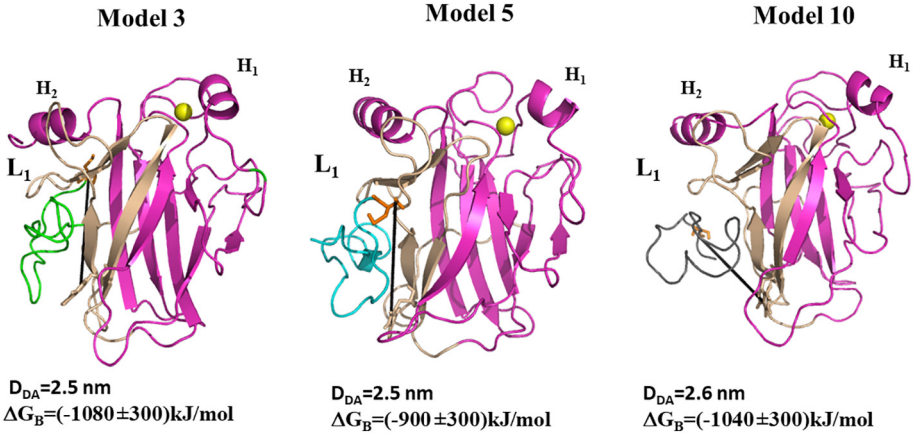

Fig. 9. Snapshot of the three best models for the DBD-p28 complex, as extracted by the docking procedure followed by a 20 ns MD simulation run. DBD is shown in magenta and light pink (COP1 binding region). p28 is in green in Model 3, in cyan in Model 5 and in grey in Model 10. The D_{DA} distance between the donor and the acceptor is marked as black line; the corresponding value, together with the binding free energy values being reported.

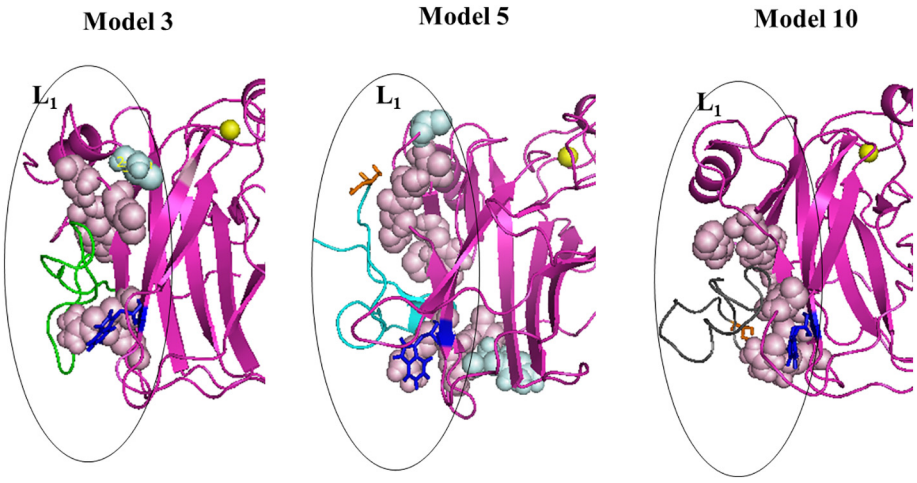

Fig. 11. A zoom view of the interacting region for the three best DBD-p28 complexes shown in Fig. 9. The DBD residues characterized by a decrease of SAS with respect to the free molecule, are marked as pink spheres for residues in a direct contact with p28 and as light blue spheres for residues non in contact. The curve (continuous line) marks the COP1 interacting region. DBD is shown in magenta, while p28 is in green in Model 3, in cyan in Model 5 and in grey in Model 10.

distance is slightly increased in Model 5 (initial value of D_{DA} = 2.4 nm) and in Model 10 (initial value of D_{DA} = 2.3 nm), while it remained unchanged in Model 3. To closely evaluate the evolution of the D_{DA} distance during the dynamics, we have performed a cluster analysis of the structures from three trajectories which give rise to the best complexes (Run 3, 5 and 10). Such an analysis has been carried out by following the all atoms RMSD with a cutoff of 0.10 nm (see Section 2.9). Along the 20 ns-long trajectories, we found 36 clusters for Run 3, 32 clusters for Run 5 and 72 clusters for Run10. The temporal evolution of the D_{DA} distance for each cluster, and for the three runs, is shown in Fig. 10. In all the cases, the distance exhibits a rather high variability during the first 10 ns; this being consistent with a structural reassessment of the two partners involved in the complex formation. At longer times, the variability is reduced with a concomitant clustering into a few structures. Such a behaviour suggests that the system moves along a restricted path towards the final bound configuration, through a clustering of the structures. Such a picture is also supported by the rather high percentage of structures, over the total, belonging to the final cluster (see the values in Fig. 10).

Notably, in all the three models, p28 is found to bind at the W region of DBD, although with slightly different orientations and arrangements. The DBD binding region of p28 appears substantially similar to that evidenced in previous docking approaches, where, however, a different initial p28 structure was used [16,55].

We have then calculated the binding free energy, ΔG_B, of these three *best models* by following the procedure described in the Materials Methods Section. The ΔG_B values, also shown in Fig. 9, have been found to be negative, and almost the same, for all the three complexes, indicating that all of them correspond to energetically favorable bound states and, therefore, they could represent the very structure of the DBD-p28 complex. In other words, our results suggest that all the three models provide a reliable description of the DBD-p28 complex; with this being in agreement with both the intrinsic structural heterogeneity of p53 and its capability to bind a variety of different ligands [1]. Consistently, it can be also hypothesized that DBD could equivalently bind slightly different structures of p28, likely present in solution [56].

The analysis of the structure of DBD-p28 complex, before and after the dynamical relaxation, has revealed that the DBD secondary structure is largely preserved in all the models, with only slight changes occurring within the terminal portions of the α-helix and β-sheets. Correspondingly, p28 undergoes some slight structural changes together with small reassessments in its position with respect to the DBD.

To analyze the interaction regions between p28 and DBD in the modelled complexes, we have compared the solvent exposed surface, evaluated by SAS, of DBD and p28, when they are free in solution or involved in the complex. Fig. 11 shows a zoom of the interacting regions for the three DBD-p28 best complexes; with the DBD residues contacting directly p28 and undergoing to a SAS decrease, being marked as pink spheres. We note that p28 binds to DBD by leaving Trp146 fully exposed to the solvent; with this being in agreement with the observed quenching of the fluorescence Trp146 band occurring without any peak shift. On the other hand, a few residues of DBD, not in direct contact with p28 (marked as light blue spheres in Fig. 11), show a SAS decrease, indicating that p28 is able to indirectly induce small reassessments of the DBD structure. Therefore, it could be conceived the fluorescence quenching of the DBD Trp146 by p28 could be due to an allosteric mechanism.

In all the three complexes, the L1 part of DBD which is involved in the binding of p53 to DNA, remains fully exposed to the solvent and then still available for a functional interaction with DNA. Such a finding supports the preservation of the DBD capability to play its functional role in gene activation, even after its binding to p28. Additionally, p28 binds to DBD with a partial coverage of the S1, L1 and S2 regions which correspond to the predicted DBD binding site for the ubiquitin ligase COP1 (light pink in Fig. 9) [57]. Accordingly, it could be hypothesized that binding of p28 to DBD could induce an inhibition of the p53 proteasome-mediated degradation driven by COP1, in agreement with what suggested in ref. [55]. Furthermore, it is interesting to note that the Ala17, Ser18, Gly19 and Tyr24 residues of p28 are always involved in the interaction with DBD. Such a finding may deserve some relevance to develop optimized drugs able to target p53.

4. Conclusions

We studied the interaction between the DNA binding domain (DBD) of the tumor suppressor p53 and the p28 peptide, in solution. Fluorescence experiments indicated the formation of a complex with an association constant of $1.35{\cdot}10^5\,M^{-1}$. Accurate FRET experiments, based on both quenching of the lone DBD tryptophan (donor), and enhancement of the IAD dye (acceptor) labelling p28, provided a value of 2.55 nm for the distance (R) between the acceptor and donor in the formed complex. By taking into account such an experimental result, we searched for the best models of the complex by a computational approach combining docking, MD simulations and free energy calculations. Among a hundred complexes, we singled out three models characterized by the lowest negative free energy and consistent with the experimental distance R. In all of these three best models, it is found that p28 competes with the p53 down-regulator COP1 for the same binding site of DBD; leaving, instead, the DNA binding site of p53 available for functional interactions. In summary, our results allowed us to elucidate the structure of the DBD-p28 complex, getting new insights into the molecular mechanisms of p28 in regulating the p53 anticancer activity, offering also new perspectives to design optimized drugs connected to the p53 anticancer function.

Author contributions

A.R.B performed modelling and data analysis, and wrote the paper. I.M. performed experiments and data analysis. S.C. designed the experiments and wrote the paper.

Funding

The paper was supported by a grant from the Italian Association for Cancer Research (AIRC No IG15866).

Disclosure statement

The authors have no conflict of interest to declare.

References

[1] B. Vogelstein, D. Lane, a J. Levine, Surfing the p53 network, Nature 408 (2000) 307–310, https://doi.org/10.1038/35042675.
[2] R.V. Sionov, I.L. Hayon, Y. Haupt, The regulation of p53 growth suppression, Cell Cycle Checkpoints Cancer, Landes Bioscience, 2002, pp. 106–125.
[3] D. Dornan, I. Wertz, H. Shimizu, D. Arnott, G.D. Frantz, P. Dowd, K. O'Rourke, H. Koeppen, V.M. Dixit, The ubiquitin ligase COP1 is a critical negative regulator of p53, Nature 429 (2004) 86–92, https://doi.org/10.1038/nature02514.
[4] C.L. Brooks, W. Gu, p53 regulation by ubiquitin, FEBS Lett. 585 (2011) 2803–2809, https://doi.org/10.1016/j.febslet.2011.05.022.
[5] K.H. Vousden, C. Prives, Blinded by the light: the growing complexity of p53, Cell 137 (2009) 413–431, https://doi.org/10.1016/j.cell.2009.04.037.
[6] O. Merkel, N. Taylor, N. Prutsch, P.B. Staber, R. Moriggl, S.D. Turner, L. Kenner, When the guardian sleeps: reactivation of the p53 pathway in cancer, Mutat. Res. 773 (2017) 1–13, https://doi.org/10.1016/j.mrrev.2017.02.003.
[7] P.A.J. Muller, K.H. Vousden, Mutant p53 in cancer: new functions and therapeutic opportunities, Cancer Cell 25 (2014) 304–317, https://doi.org/10.1016/j.ccr.2014.01.021.
[8] A. Friedler, L.O. Hansson, D.B. Veprintsev, S.M.V. Freund, T.M. Rippin, P.V. Nikolova, M.R. Proctor, S. Rüdiger, A.R. Fersht, A peptide that binds and stabilizes p53 core domain: chaperone strategy for rescue of oncogenic mutants, Proc. Natl. Acad. Sci. U. S. A. 99 (2002) 937–942, https://doi.org/10.1073/pnas.241629998.
[9] F. Domenici, M. Frasconi, F. Mazzei, G. D'Orazi, A.R. Bizzarri, S. Cannistraro, Azurin modulates the association of Mdm2 with p53: SPR evidence from interaction of the full-length proteins, J. Mol. Recognit. 24 (2011) 707–714, https://doi.org/10.1002/jmr.1105.
[10] G. Funari, F. Domenici, L. Nardinocchi, R. Puca, G. D'Orazi, A.R. Bizzarri, S. Cannistraro, Interaction of p53 with Mdm2 and azurin as studied by atomic force spectroscopy, J. Mol. Recognit. 23 (2010) 343–351. doi:https://doi.org/10.1002/jmr.999
[11] V. Punj, T.K. Das Gupta, A.M. Chakrabarty, Bacterial cupredoxin azurin and its interactions with the tumor suppressor protein p53, Biochem. Biophys. Res. Commun. 312 (2003) 109–114, https://doi.org/10.1016/j.bbrc.2003.09.217.
[12] T. Yamada, Y. Hiraoka, M. Ikehata, K. Kimbara, B.S. Avner, T.K. Das Gupta, A.M. Chakrabarty, Apoptosis or growth arrest: modulation of tumor suppressor p53's specificity by bacterial redox protein azurin, Proc. Natl. Acad. Sci. U. S. A. 101 (2004) 4770–4775, https://doi.org/10.1073/pnas.0400899101.
[13] T. Yamada, M. Goto, V. Punj, O. Zaborina, M.L. Chen, K. Kimbara, D. Majumdar, E. Cunningham, T.K. Das Gupta, A.M. Chakrabarty, Bacterial redox protein azurin, tumor suppressor protein p53, and regression of cancer, Proc. Natl. Acad. Sci. U. S. A. 99 (2002) 14098–14103, https://doi.org/10.1073/pnas.222539699.
[14] T. Yamada, T.K. Das Gupta, C.W. Beattie, p28-mediated activation of p53 in G2–M phase of the cell cycle enhances the efficacy of DNA damaging and antimitotic chemotherapy, Cancer Res. 76 (2016) 2354–2365, https://doi.org/10.1158/0008-5472.CAN-15-2355.
[15] A.R. Bizzarri, S. Santini, E. Coppari, M. Bucciantini, S. Di Agostino, T. Yamada, C.W. Beattie, S. Cannistraro, Interaction of an anticancer peptide fragment of azurin with p53 and its isolated domains studied by atomic force spectroscopy, Int. J. Nanomedicine 6 (2011) 3011–3019, https://doi.org/10.2147/IJN.S26155.
[16] S. Santini, A.R. Bizzarri, S. Cannistraro, Modelling the interaction between the p53 DNA-binding domain and the p28 peptide fragment of Azurin, J. Mol. Recognit. 24 (2011) 1043–1055, https://doi.org/10.1002/jmr.1153.
[17] S. Signorelli, S. Santini, T. Yamada, A.R. Bizzarri, C.W. Beattie, S. Cannistraro, Binding of amphipathic cell penetrating peptide p28 to wild type and mutated p53 as studied by Raman, atomic force and surface plasmon resonance spectroscopies, Biochim. Biophys. Acta Gen. Subj. 1861 (2017) 910–921, https://doi.org/10.1016/j.bbagen.2017.01.022.
[18] I. Moscetti, S. Cannistraro, A.R. Bizzarri, Surface plasmon resonance sensing of biorecognition interactions within the tumor suppressor P53 network, Sensors (Switzerland). 17 (2017) 2680, https://doi.org/10.3390/s17112680.
[19] S. Santini, A.R. Bizzarri, S. Cannistraro, Revisitation of FRET methods to measure intraprotein distances in Human Serum Albumin, J. Lumin. 179 (2016) 322–327, https://doi.org/10.1016/j.jlumin.2016.07.029.
[20] D.S. Logvinova, D.I. Markov, O.P. Nikolaeva, N.N. Sluchanko, D.S. Ushakov, D.I. Levitsky, Does interaction between the motor and regulatory domains of the myosin head occur during ATPase cycle? evidence from thermal unfolding studies on myosin sbfragment 1, PLoS One 10 (2015) e0137517, , https://doi.org/10.1371/journal.pone.0137517.
[21] Y. Cho, S. Gorina, P.D. Jeffrey, N.P. Pavletich, Crystal structure of a p53 tumor suppressor-DNA complex: understanding tumorigenic mutations, Science 265 (1994) 346–355, https://doi.org/10.1126/science.8023157.
[22] J. Duan, L. Nilsson, Effect of Zn2+ on DNA recognition and stability of the p53 DNA-binding domain, Biochemistry 45 (2006) 7483–7492, https://doi.org/10.1021/bi0603165.
[23] V. De Grandis, A.R. Bizzarri, S. Cannistraro, Docking study and free energy simulation of the complex between p53 DNA-binding domain and azurin, J. Mol. Recognit. 20 (2007) 215–226, https://doi.org/10.1002/jmr.840.
[24] H. Nar, A. Messerschmidt, R. Huber, M. Van De Kamp, G.W. Canters, Crystal structure of *Pseudomonas aeruginosa* apo-azurin at 1.85 A resolution, FEBS Lett. 306 (1992) 119–124, https://doi.org/10.1016/0014-5793(92)80981-L.
[25] N. Guex, M.C. Peitsch, SWISS-MODEL and the Swiss-PdbViewer: an environment for comparative protein modeling, Electrophoresis 18 (1997) 2714–2723.
[26] S. Signorelli, S. Santini, T. Yamada, A.R. Bizzarri, C.W. Beattie, S. Cannistraro, Binding of amphipathic cell penetrating peptide p28 to wild type and mutated p53 as studied by Raman, atomic force and surface plasmon resonance spectroscopies, Biochim. Biophys. Acta - Gen. Subj. 1861 (2017) 910–921, https://doi.org/10.1016/j.bbagen.2017.01.022.
[27] T. Yamada, S. Signorelli, S. Cannistraro, C.W. Beattie, A.R. Bizzarri, Chirality switching within an anionic cell-penetrating peptide inhibits translocation without affecting preferential entry, Mol. Pharm. 12 (2015) 140–149, https://doi.org/10.1021/mp500495u.
[28] B.G. Pierce, K. Wiehe, H. Hwang, B.H. Kim, T. Vreven, Z. Weng, ZDOCK server: interactive docking prediction of protein-protein complexes and symmetric multimers, Bioinformatics 30 (2014) 1771–1773, https://doi.org/10.1093/bioinformatics/btu097.
[29] M.J. Abraham, T. Murtola, S.P. Schulz, Roland Shultz, J.C. Smith, B. Hess, E. Lindah, Gromacs: High performance molecular simulations through multi-level parallelism from laptops to supercomputers, SoftwareX. 1–2 (2015) 19–25, https://doi.org/10.1016/j.softx.2015.06.001.
[30] B. Hess, C. Kutzner, D. Van Der Spoel, E. Lindahl, GROMACS 4: Algorithms for highly efficient, load-balanced, and scalable molecular simulation, J. Chem. Theory Comput. 4 (2008) 435–447, https://doi.org/10.1021/ct700301q.
[31] I. van Gunsteren, W.F. Billeter, S.R. Eking, A.A. Hiinenberger, P.H. Kriiger, P. Mark, A.E. Scott, W.R.P. Tironi, Biomolecular Simulation, The GROMOS96 Manual and User Guide, (1996).
[32] H.J.C. Berendsen, J.R. Grigera, T.P. Straatsma, The missing term in effective pair potentials, J. Phys. Chem. 91 (1987) 6269–6271, https://doi.org/10.1021/j100308a038.
[33] K. Kholmurodov, MD simulations of the P53 oncoprotein structure: the effect of the Arg273→his mutation on the DNA binding domain, Adv. Biosci. Biotechnol. 02 (2011) 330–335, https://doi.org/10.4236/abb.2011.25048.
[34] T. Darden, D. York, L. Pedersen, Particle mesh Ewald: an N·log(N) method for Ewald sums in large systems, J. Chem. Phys. 98 (1993) 10089–10092, https://doi.org/10.1063/1.464397.
[35] B. Hess, H. Bekker, H.J.C. Berendsen, J.G.E.M. Fraaije, LINCS: a linear constraint solver for molecular simulations, J. Comput. Chem. 18 (1997) 1463–1472, https://doi.org/10.1002/(SICI)1096-987X(199709)18:12<1463::AID-JCC4>3.0.CO;2-H.
[36] S. Nosé, A unified formulation of the constant temperature molecular dynamics methods, J. Chem. Phys. 81 (1984) 511–519, https://doi.org/10.1063/1.447334.
[37] M. Parrinello, A. Rahman, Polymorphic transitions in single crystals: a new molecular dynamics method, J. Appl. Phys. 52 (1981) 7182–7187, https://doi.org/10.1063/1.328693.
[38] W.F. Humphrey, A. Dalke, K. Schulten, VMD—visual molecular dynamics, J. Mol. Graph. 14 (1996) 33–38.
[39] W. Kabsch, C. Sander, Dictionary of protein secondary structure: pattern recognition of hydrogen bonded and geometrical features, Biopolymers 22 (1983) 2577–2637, https://doi.org/10.1002/bip.360221211.
[40] J. Srinivasan, T.E. Cheatham, P. Cieplak, P.A. Kollman, D.A. Case, Continuum Solvent Studies of the Stability of DNA, RNA, and Phosphoramidate−DNA Helices, J. Am. Chem. Soc. 120 (1998) 9401–9409, https://doi.org/10.1021/ja981844.
[41] V. De Grandis, A.R. Bizzarri, S. Cannistraro, Docking study and free energy simulation of the complex between p53 DNA-binding domain and azurin, J. Mol. Recognit. 20 (2007), https://doi.org/10.1002/jmr.840.
[42] M. Taranta, A.R. Bizzarri, S. Cannistraro, Modeling the interaction between the N-terminal domain of the tumor suppressor p53 and azurin, J. Mol. Recognit. 22 (2009), https://doi.org/10.1002/jmr.934.
[43] N. Basdevant, H. Weinstein, M. Ceruso, W. Medical, C. Uni, A.V. York, N. York, N. York, Thermodynamic Basis for Promiscuity and Selectivity in Protein - Protein Interactions : PDZ Domains , A Case Study, 9 (2006), pp. 12766–12777.
[44] S. Santini, A.R. Bizzarri, S. Cannistraro, Modelling the interaction between the p53 DNA-binding domain and the p28 peptide fragment of Azurin, J. Mol. Recognit. 24 (2011), https://doi.org/10.1002/jmr.1153.
[45] P.A. Kollman, I. Massova, C. Reyes, B. Kuhn, S. Huo, L. Chong, M. Lee, T. Lee, Y. Duan, W. Wang, O. Donini, P. Cieplak, J. Srinivasan, D.A. Case, T.E. Cheatham, Calculating structures and free energies of complex molecules: Combining molecular mechanics and continuum models, Acc. Chem. Res. 33 (2000) 889–897, https://doi.org/10.1021/ar000033j.
[46] Y. Wu, Z. Cao, H. Yi, D. Jiang, X. Mao, H. Liu, W. Li, Simulation of the interaction between ScyTx and small conductance calcium-activated potassium channel by

docking and MM-PBSA, Biophys. J. 87 (2004) 105–112, https://doi.org/10.1529/biophysj.103.039156.
[47] A. Ganoth, R. Friedman, E. Nachliel, M. Gutman, A molecular dynamics study and free energy analysis of complexes between the Mlc1p protein and two IQ motif peptides, Biophys. J. 91 (2006) 2436–2450, https://doi.org/10.1529/biophysj.106.085399.
[48] L.T. Chong, Y. Duan, L. Wang, I. Massova, P. a Kollman, Molecular dynamics and free-energy calculations applied to affinity maturation in antibody 48G7, Proc. Natl. Acad. Sci. U. S. A. 96 (1999) 14330–14335, https://doi.org/10.1073/pnas.96.25.14330.
[49] X. Daura, K. Gademann, B. Jaun, D. Seebach, W.F. van Gunsteren, A.E. Mark, Peptide folding: when simulation meets experiment, Angew. Chemie Int. Ed. 38 (1999) 236–240, https://doi.org/10.1002/(SICI)1521-3773(19990115)38:1/2<236::AID-ANIE236>3.3.CO;2-D.
[50] J.R. Lakowicz, Principles of Fluorescence Spectroscopy, 3rd ed., Springer US, 2006.
[51] S. Santini, A.R. Bizzarri, T. Yamada, C.W. Beattie, S. Cannistraro, Binding of azurin to cytochrome c 551 as investigated by surface plasmon resonance and fluorescence, J. Mol. Recognit. 27 (2014), https://doi.org/10.1002/jmr.2346.
[52] S. Santini, A.R. Bizzarri, S. Cannistraro, Revisitation of FRET methods to measure intraprotein distances in Human Serum Albumin, J. Lumin. 179 (2016), https://doi.org/10.1016/j.jlumin.2016.07.029.
[53] P. Wu, L. Brand, Conformational flexibility in a staphylococcal nuclease mutant K45C from time-resolved resonance energy transfer measurements, Biochemistry 33 (1994) 10457–10462.
[54] N.H.I. Medintz, FRET – Förster Resonance Energy Transfer From Theory to Applications, Wiley-VCHVerlag, Weinheim, 2014, https://doi.org/10.1002/9783527656028.ch03.
[55] T. Yamada, K. Christov, A. Shilkaitis, L. Bratescu, A. Green, S. Santini, A.R. Bizzarri, S. Cannistraro, T.K.D. Gupta, C.W. Beattie, p28, a first in class peptide inhibitor of cop1 binding to p53, Br. J. Cancer 108 (2013) 2495–2504, https://doi.org/10.1038/bjc.2013.266.
[56] T. Yamada, S. Signorelli, S. Cannistraro, C.W. Beattie, A.R. Bizzarri, Chirality switching within an anionic cell-penetrating peptide inhibits translocation without affecting preferential entry, Mol. Pharm. 12 (2015), https://doi.org/10.1021/mp500495u.
[57] D.-Q. Li, S. Divijendra Natha Reddy, S.B. Pakala, X. Wu, Y. Zhang, S.K. Rayala, R. Kumar, MTA1 coregulator regulates p53 stability and function, J. Biol. Chem. 284 (2009) 34545–34552, https://doi.org/10.1074/jbc.M109.056499.